NUMERICAL INVESTIGATION OF EFFUSION COOLING AIR INFLUENCE ON THE CO EMISSIONS FOR A SINGLE-SECTOR AERO-ENGINE MODEL COMBUSTOR

Sandra Recio Balmaseda [†*]
Tim Jeremy Patrick Karpowski [†]
Hendrik Nicolai
Philipp Koob
Christian Hasse
Institute for Simulation of reactive Thermo-Fluid Systems
Technical University Darmstadt
Otto-Berndt-Straße 2,
64287 Darmstadt, Germany
e-mail: recio@stfs.tu-darmstadt.de

Max Greifenstein
Andreas Dreizler
Institute for Reactive Flows and Diagnostics
Technical University Darmstadt
Otto-Berndt-Straße 3,
64287 Darmstadt, Germany

ABSTRACT

Stricter aviation emissions regulations have led to the desire for lean-premixed-vaporized combustors over rich-quench-lean burners. While this operation mode is beneficial for reducing NOx and particulate emissions, the interaction of the flame and hot exhaust gases with the cooling flow results in increased CO emissions. Predicting CO in computational fluid dynamics (CFD) simulations remains challenging. To assess current model performance under practically relevant conditions, Large-Eddy Simulation (LES) of a lab-scale effusion cooling test rig is performed. Flamelet-based manifolds, in combination with the Artificial Thickened Flame (ATF) approach, are utilized to model the Turbulence-Chemistry Interaction (TCI) in the test-rig with detailed chemical kinetics at reduced computational costs. Heat losses are considered via exhaust gas recirculation (EGR). Local transport effects in CO emissions are included through an additional transport equation. Additionally, a Conjugate Heat Transfer (CHT) simulation is performed for good estimations of the thermal boundary conditions. Extensive validation of this comprehensive model is conducted using the available experimental dataset for the studied configuration. Subsequently, model sensitivities for predicting CO are assessed, including the progress variable definition and the formulation of the CO source term in the corresponding transport equation. To investigate the flame thickening influence in the calculated CO, an ATF-postprocessing correction is further developed. Integrating multiple sophisticated pollutant submodels and evaluating their sensitivity offers insights for future investigations into modeling CO emissions in aero-engines and stationary gas turbines.

[†]Joint first authors
[*]Address all correspondence to this author

NOMENCLATURE

Latin Letters

a, b	ATF correction factors
C_p	heat capacity at constant pressure
$\mathscr{E}$	efficiency function
$\mathscr{F}$	thickening factor
h	enthalpy
$\dot{m}$	mass flux
p	pressure
Sc_t	turbulent Schmidt number
T	temperature
t	time
U	velocity
$x_{(i)}$, y, z	spacial coordinate
X_i	mole fraction
Y_c	progress variable
Y_i	mass fraction of species i
Z	mixture fraction
z_w	distance over the effusion cooling wall

Greek Letters

ρ	density
μ_t	turbulent viscosity
λ	thermal conductivity
φ	equivalence ratio
ϕ	control variables
Ξ	wrinkling factor

$\dot{\omega}_i$	source term of species i
Ω	flame sensor

Super- and subscripts

$^{\pm}$	split into production and destruction term
^{table}	table look-up quantity
^{tr}	transported quantity
^{c}	(ATF)-laminar post-correction
^{c,T}	(ATF)-turbulence post-correction

Abbreviations

ATF	Artificial Thickened Flame
CFD	Computational Fluid Dynamics
CHT	Conjugate Heat Transfer
EGR	Exhaust Gas Recirculation
FCAI	Flame-Cooling Air Interaction
FWI	Flame-Wall Interaction
FPF	Freely Propagating Flame
IRZ	Inner Recirculation Zone
ISL	Inner Shear Layer
LES	Large Eddy Simulation
LPP	Lean-Premixed-Vaporized
ORZ	Outer Recirculation Zone
OSL	Outer Shear Layer
RMS	Root-Mean-Square
RQL	Rich-Quench-Lean
TCI	Turbulence Chemistry Interaction

1. INTRODUCTION

Air traffic, a critical source of pollutant emissions, has continued to grow in the past 30 years. It is expected to double in size by the mid-2030s [1]. This scenario strongly contrasts the emission goals declared in “Flightpath 2050" [2]. Substantial improvements to the existing aero-engines are required to achieve these goals. With this purpose, Computational Fluid Dynamics (CFD) has become an indispensable tool in developing future aero-engine designs [3]. Nevertheless, simulating aero-engine combustion chambers under realistic operating conditions is challenging due to the intricate interplay of complex combustion phenomena, including turbulence-chemistry interaction (TCI), transient conditions, and effusion-cooled walls [4]. The difficulties extend to designing experimental setups for data validation at high pressures and temperatures.

Previously, the combination of flamelet-based tabulated manifolds coupled with Large-Eddy Simulation (LES) showed success in developing rich-quench-lean (RQL) burners [5–7]. To decrease NO_x emissions through lower peak temperatures and comply with the “Flightpath 2050" goals, it is advantageous to change from RQL to a lean-premixed-vaporized (LPP) concept [8]. However, LPP burners imply an increased demand for effusion cooling due to the higher thermal loads on the combustor walls [9, 10]. This affects the predictability of the current manifold models, as the cooling flow interaction with the flame is known to increase CO emissions [11] through chemical quenching and mixing-enhanced processes with the exhaust gases. The process is dominated by dilution and higher mixing with the cooling air when moving downstream with an increment of effusion cooling holes in the axial direction, provoking a decline in CO concentrations and temperature. This was demonstrated in recent experiments performed in an effusion-cooled single-sector model gas turbine combustor [12–15]. The measured thermo-chemical states (characterized by CO mole fraction and temperature) revealed a substantial influence of the effusion cooling flow on the lean-flame chemistry.

Capturing all these processes in the simulation is challenging due to the high sensitivity of CO to the local combustion regime and heat losses. Generally, model extensions are required to capture these combustion effects accurately [6, 16, 17], but their combined utilization in effusion-cooled chambers is yet to be performed.

In general, tabulated manifolds in the literature are based on 1D freely propagating flames (FPF) [18, 19]. Popp et al. [5, 6] validated this standard tabulation approach for premixed and diffusion flames in a multi-regime burner setup. The local combustion regime effects combined with recirculation zones and their influence on CO emissions were analyzed. It was found that the premixed flamelet-based manifolds can correctly capture temperature and major species trends. However, larger discrepancies are reported for minor species such as CO, which is highly affected by local transport processes. Solving an additional transport equation for CO [20] improved the results significantly compared to direct lookup from the manifold, as also observed in [16, 21] in more generic configurations.

In realistic configurations, heat loss effects must be accounted for in the combustion chemistry, especially for the prediction of minor species and pollutants such as CO. Thus, improved manifolds, which consider enthalpy as a third table dimension, are needed [16, 17]. The reason is the diffusion of CO towards lower enthalpy levels. Heat losses can happen due to flame quenching to the wall or due to mixing with cooling air. Several authors have addressed numerically the influence of heat losses due to cooled walls on the global flow field solution. Ketelheun et al. [22] implemented enthalpy variation through exhaust gas recirculation (EGR) in wall-enclosed flames. The author could observe cooling effects not captured by the standard manifolds and a better agreement in the main combustion zone with the experimental data. However, wall heat transfer was still underestimated. This flame quenching phenomenon was addressed in more detail in academic flame-wall interaction (FWI) configurations [16, 17, 21].

In the case of flame-cooling air interaction (FCAI), significantly less work has been performed. According to Palulli et al. [23], who studied FCAI in a generic configuration, depending on the combustor geometry and combustion mode, both FWI and FCAI can take place inside the combustor. While both lead to an increase in exhaust CO emissions, depending on which phenomenon dominates, there would be a predominance of either quenching or mixing and dilution effects. The combustion

modeling strategy would need to be adjusted accordingly [24]. At higher cooling rates, the $Y_{CO} - T$ dependency could be properly featured by 1D FPF solutions in an a-priori analysis [23, 24].

The previous studies offered an overview of the influence of different parameters in generic FCAI scenarios. However, no further numerical analysis was performed on the FCAI influence on CO emissions and the modeling strategy required to capture all these physical effects properly in closer-to-reality aero-engine conditions. It is still unclear if the EGR extension for heat losses in the flamelet manifold is enough to capture the combustion chemistry in the FCAI zone or if the effect of surrounding non-adiabatic walls is still significant and further model extensions, e.g., flame quenching are required. In the experimental field, the effusion-cooled single-sector gas turbine combustor previously investigated by Hermann, Greifenstein et al. [12, 14, 25] is a suitable configuration towards FCAI relevant-industry set-ups. It provides accurate FCAI boundary conditions and comprehensive validation data, both for the global flow field and thermo-chemical states. Amerini et al. [26] simulated this combustor to assess their loosely-coupled Conjugate Heat Transfer (CHT) approach with tabulated chemistry for adiabatic flamelets. These authors demonstrated that their modeling strategy was capable of capturing the general flowfield characteristics. However, a detailed numerical analysis of CO evolution, especially with the cooling flow in the FCAI zone and its sensitivity to model extensions, has not been performed yet.

The objective of this work is to assess the effect of current CFD model capabilities for predicting the complex thermo-chemical states during FCAI in a practically relevant aero-engine scenario. The capabilities of the employed flamelet manifolds to predict CO emissions evolution along the chamber are evaluated. In particular, the use of EGR flamelet manifolds is validated against the available detailed experimental measurements in an FCAI-dominant scenario. In addition, improvements in modeling strategies, namely a transport equation for CO, split and linear correction of the CO source term within, and an ATF post-processing correction, are validated with experimental data. Their interaction with the progress variable definition, as well as the benefits and shortcomings of the tested model extensions, are highlighted.

The remainder of this work is structured as follows: first, the experimental setup is introduced. Subsequently, the employed combustion models and numerical set-up are presented. In the results section, first, the simulations are compared to the experimental data in terms of temperature and velocity, and then the CO predictions are discussed. In the end, a conclusion is given.

2. EXPERIMENTAL SETUP

A schematic of the studied burner, including the used coordinate system, is shown in Fig. 1. The burner is enclosed in a pressure vessel but still enables optical access from the top and the sides of the burner through glass windows. Preheated air and natural gas are premixed in a plenum before a movable block swirler,

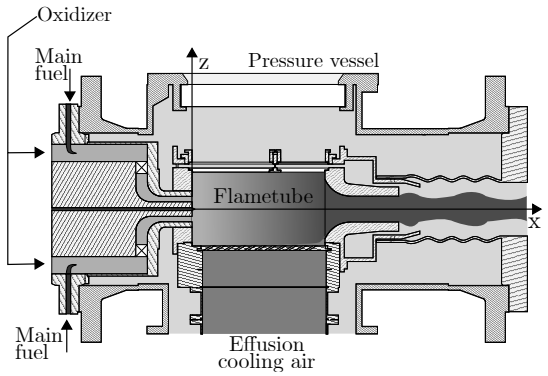

FIGURE 1: SCHEMATIC OF THE EXPERIMENTAL SETUP, ADAPTED FROM [13].

which is based on the well-known TECFLAM design [27]. A modular effusion plate is mounted at the bottom of the chamber. All mass flows entering the combustor are individually conditioned and controlled using thermal mass flow controllers. In this study, the low swirl, high cooling, fully premixed condition is investigated. The parameters of this operating condition are summarized in Tab. 1. This operating condition features high CO emissions and represents the highest FCAI interaction among the measured operating conditions. As a consequence, mixing, dilution, and chemical quenching effects due to the interaction of the flame and hot exhaust gases with the cooling air are expected to dominate over heat loss and thermal quenching to the wall.

TABLE 1: INVESTIGATED OPERATING CONDITIONS FROM [13].

Name	Symbol	Main	Cooling	Unit
Mass flow	$\dot{m}_{\mathrm{ox/eff}}$	30	15	g/s
Temperature	$T_{\mathrm{ox/eff}}$	623	623	K
Equivalence ratio	φ	0.75	0	-
Operating pressure	p	0.25	0.25	MPa
Swirl number	S	0.7	-	-

Particle Image Velocimetry (PIV) measurements were performed in [25]. The measured velocities are recorded for an equivalence ratio $\varphi = 0.65$. For the velocity comparison, a simulation with an adapted equivalence ratio is performed.

Gas phase temperature and CO mole fractions X_{CO} measurements of the studied operating condition are available for $\varphi = 0.75$ [14]. The temperature was measured with coherent anti-Stokes Raman spectroscopy (CARS), while X_{CO} was measured with quantitative CO two-photon laser-induced fluorescence (CO-LIF).

For the studied operating point, no measurements of the wall temperatures exist. In Greifenstein et al. [12], measurements of the effusion cooling plate temperature exist for $\varphi = 0.65$, which only gives a qualitative comparison to the here studied condition, $\varphi = 0.75$.

3. COMBUSTION MODEL

In the following, an overview of the employed modeling strategies as well as model improvements for capturing CO accurately, are outlined.

3.1 Standard flamelet-manifold methodology

The basis for the combustion model is the commonly employed flamelet-based tabulation method [18, 19].

In the first step, adiabatic freely propagating flamelets with varying mixture fractions are computed with the flame solver Cantera [28] using a unity Lewis number for all species. This modeling approach has continued to be employed in CH_4-air turbulent flame works of relevance [6, 29, 30].

The chemical kinetics are modeled through the GRI-3.0 detailed mechanism (53 species and 325 reactions) [31]. Subsequently, the calculated flamelets are parameterized by the mixture fraction Z and the progress variable Y_c. For the tabulation, 200 points were set for the mixture fraction, keeping a refined resolution $\Delta Z = 0.001$ in the flammable range for this set-up, and 100 points for the progress variable. Two progress variable definitions were considered: $Y_{c,1} = CO_2$ and $Y_{c,2} = CO_2 + H_2O + CO$.

3.2 Heat losses implementation in the manifolds

Standard flamelet-based manifolds are unable to represent the high CO diffusion in the direction of decreasing enthalpy levels from the adiabatic region [16]. Given that heat losses are expected in the current FCAI configuration, it is necessary to extend the tabulation strategy by including the enthalpy dimension. Due to the operating point considered with the highest cooling mass flow rate, it is expected that mixing, dilution, and chemical quenching effects due to the cooling flow influence dominate over flame quenching to the wall. Under this presumption, EGR flamelet manifolds would be suitable to model the set-up physics [22, 32, 33]. They are generated from a series of independent one-dimensional freely propagating flames with varying enthalpy levels as proposed by Fiorina et al. [34].
Enthalpy reduction is achieved by exhaust gas recirculation, that is, different amounts of cooled burned gases are added to the inflow mixture of the flame [35, 36]. Additionally, the upper enthalpy limit is expanded using one-dimensional freely propagating flames with increased inflow temperatures.

In the range between $Z_{\min}$ and pure oxidizer ($Z = 0$), the thermo-chemical states from the last flammable mixture and pure oxidizer are interpolated [22]. The simulation results are mapped on a normalized state space $\Phi = \Phi^{\text{table}}(Z, C_n, H_n)$, with the normalized progress variable C_n and enthalpy H_n. The manifold final dimensions are $200 \times 100 \times 100$.

3.3 Local transport effects for CO

A CO-transport equation to account for the local transport phenomena [20, 21] is implemented

$$\frac{\partial \rho Y_{\text{CO}}}{\partial t} + \frac{\partial}{\partial x_i}\left(\rho U Y_{\text{CO}}\right) = \frac{\partial}{\partial x_i}\left(\frac{\lambda}{C_p} + \frac{\mu_t}{Sc_t}\right)\frac{\partial Y_{\text{CO}}}{\partial x_i} + \dot{\omega}_{\text{CO}} \quad (1)$$

with λ the thermal conductivity, C_p the heat capacity at constant pressure, μ_t the turbulent viscosity, $Sc_t = 0.7$ the turbulent Schmidt number and $\dot{\omega}_{CO}$ the chemical source term. This allows the CO mass fraction to evolve according to its own time scale, considering possible perturbations due to the effect of transport terms [5, 6]. The flamelet-based tabulation approach relies on the fast-chemistry assumption. It is able to provide an accurate prediction of the individual species trends as long as their time scales are of smaller or the same order when compared to the time scale of the selected progress variable. As discussed by Popp et al. [6], complex flow and recirculation structures can lead to discrepancies between the tabulated and transported CO timescales. The introduction of an additional transport equation for slowly reacting species was pioneered for NO formation by Ihme and Pitsch [37] and Ketelheun et al. [38]. Derived from a timescale analysis highlighting the relatively slow NO formation compared to the flamelet lifetime, this concept was later applied by Mueller et al. [39] to address slow polycyclic aromatic hydrocarbons (PAH) species for soot formation. The additional transport equation for CO was implemented in the works of Ganter et al. [21] and Han et al. [20] to enhance the representation of CO formation by accounting for the local transport phenomena.

The last term on the right-hand side refers to the chemical source term, which receives a special treatment [16, 19].

The value $\dot{\omega}_{\text{CO}}^{\text{table}}$ looked up from the manifold is corrected linearly to account for a changed transported CO mass fraction, $Y_{\text{CO}}^{\text{tr}}$, as compared to its local value at the manifold, $Y_{\text{CO}}^{\text{table}}$. The total source term $\dot{\omega}_{\text{CO}}$ is split into production and consumption

$$\dot{\omega}_{\text{CO}} = \dot{\omega}_{\text{CO}}^{+} + Y_{\text{CO}}^{tr}\left(\frac{\dot{\omega}_{\text{CO}}^{-}}{Y_{\text{CO}}^{table}}\right). \quad (2)$$

3.4 Artificial Thickened Flame approach

The subgrid-scale turbulence-chemistry interaction (SGS-TCI) closure is considered through the Artificial Thickened Flame approach (ATF) as used in [40]. The ATF model is based on a coordinate transformation that is applied to the scalar transport equation to thicken the flame front and, as a consequence, make it resolvable on coarse LES grids. For each control variable, $\phi = [Z, Y_c, h]$, the modified transport equation reads

$$\frac{\partial \rho \phi}{\partial t} + \frac{\partial}{\partial x_i}\left(\rho U \phi\right) = \frac{\partial}{\partial x_i}\left(\mathcal{F}\mathcal{E}\frac{\lambda}{C_p} + (1-\Omega)\frac{\mu_t}{Sc_t}\right)\frac{\partial \phi}{\partial x_i} + \frac{\mathcal{E}}{\mathcal{F}}\dot{\omega}_\phi \quad (3)$$

with $\mathcal{F}$ the effective thickening factor, $\mathcal{E}$ the effective efficiency function [41] , Ω the flame sensor, and $\dot{\omega}_\phi$ the scalar source term. In the context of ATF, a dynamic thickened flame approach with grid-adaptive thickening following [42] is employed, in combination with the flame sensor definition $\Omega = 16[Y_c(Y_c - 1)]^2$ [43]. In the flame front, $n = 5$ points is selected, which is validated with 1D flame simulations at the corresponding operating conditions. The efficiency function by Charlette et al. [41] with a static constant $\beta = 0.5$ and a Kolmogorov constant $C_k = 1.5$ was used.

3.5 CO post-processing correction for ATF

When performing ATF for the TCI closure, it is found that species profiles such as CO are overestimated [30]. First, in laminar flames, ATF thickens species profiles. This means that the total mass of species is overpredicted. This is shown in Fig. 2, where the mean flame brush was generated by shifting 10.000 1D flamelets assuming a uniform spatial distribution following [44], to mimic the impact on time-averaged flames. Here $< Y_{CO} >$ marks the time-averaged thickened CO profile. Gruhlke et al. [45] proposed a laminar flame thickening correction for the time-averaged profiles of species mass fractions Y_k^c.

$$< \hat{Y}_k^c \left(x^*\right) >=< \hat{Y}_k \left(x^*\right) / \mathcal{F} \left(x^*\right) > \tag{4}$$

In turbulent flames, besides presenting the previous issue, the thickening of the flame neglects the impact of sub-filter scale flame wrinkling on the filtered chemical flame structure. As discussed in [46], this leads to a 50 % underestimation of CO peak under the given conditions as seen in Fig. 2 as $< Y_{CO}^c >$. Mercier et al. [47] proposed a correction based on manufactured filtered wrinkled flamelets (FWF) to account for the impact of subgrid-scale flame wrinkling on species production. In order to incorporate it into the thickened flame framework, it is necessary to correct the previous laminar correction Y_k^c with an empirical wrinkling factor

$$\hat{Y}_k^{c,T} \left(x^*\right) = \hat{Y}_k^c \left(x^*\right) \left(a\Xi + b\right). \tag{5}$$

The coefficients a and b can be estimated from FWF elements as shown in [45]. As the current correction is empirical, the values of Eq. (5) need to be evaluated for the selected progress variables and studied operating conditions. In this study, the values are determined to be $a = 0.816$ and $b = 0.191$ for $Y_{c,1}$, and $a = 0.650$ and $b = 0.375$ for $Y_{c,2}$, respectively. For more complex partially premixed cases, the parameters could be included in the flamelet table to account for the changing conditions. In Fig. 2, a comparison between the original thickened profiles, the ones with laminar correction, and the ones with turbulent correction applied on the transported CO profiles is presented for both progress variable definitions at the corresponding conditions.

As it can be noticed, $Y_{c,2}$, used in the previous works [45, 47], shows a better match with the unthickened flame solution in Fig. 2. This might be due to the incorporation of CO in the progress variable definition, which could favor $Y_{c,2}$ in this artificially generated solution. However, in the coupled simulation, $Y_{c,1}$ provides a better flame resolution, as well as a better alignment with the selected flame sensor (see Fig. 3), thus both definitions are evaluated. To the authors' best knowledge, this is the first time a CO transport equation is solved in conjunction with a three-dimensional table including heat losses with ATF closure. Contrary to previous works [30, 45], this correction is applied to the transported CO instead of to the species tabulated values.

4. SOLVER AND NUMERICAL SETUP

In this section, the utilized solver and numerical setup are presented. First, the setup for the fluid flow solver is described.

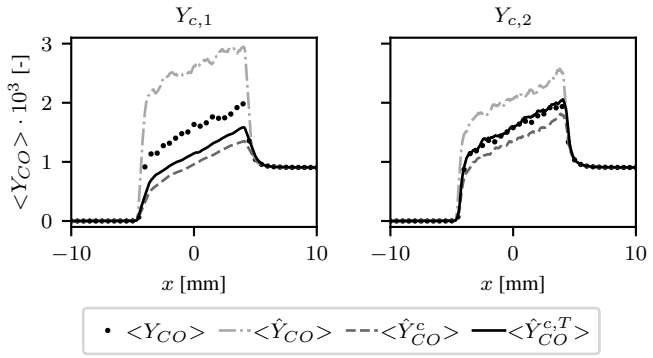

FIGURE 2: AVERAGED PROFILES OF CO MASS FRACTION MIMICKING THE FLAME BRUSH FOR THE PROGRESS VARIABLES $Y_{c,1}$ AND $Y_{c,2}$. $< Y_{CO} >$ (LAMINAR), $< \hat{Y}_{CO} >$ (THICKENED), $< \hat{Y}_{CO}^c >$ (THICKENED, LAMINAR CORRECTION), $< \hat{Y}_{CO}^{c,T} >$ (THICKENED, TURBULENT CORRECTION).

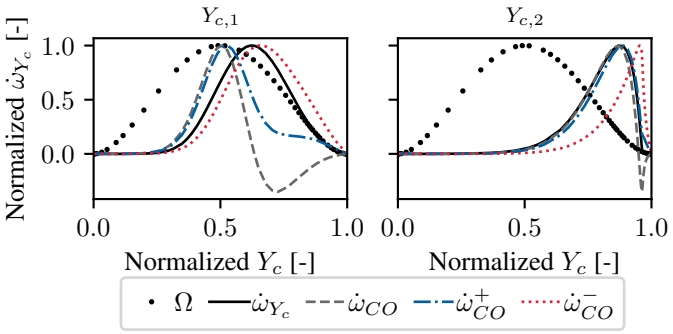

FIGURE 3: ALIGNMENT OF THE FLAME SENSOR [43] WITH THE PROGRESS VARIABLES AND CO SOURCE TERMS.

Afterwards the employed CHT approach is shortly presented.

4.1 Fluid solver

LES of the effusion cooling test-rig is performed within an OpenFOAM [48] in-house framework [6], using 2nd- order discretization in time and space and a pressure-based algorithm to solve the Favre-filtered Navier-Stokes equations in the low Mach number formulation. For brevity, the filtering operator $\tilde{}$ is omitted throughout, as only Favre-filtered quantities are discussed. The non-resolved subgrid viscosity is modeled using the σ-model by Nicoud et al. [49] with a model constant of $C_\sigma = 1.5$. The LES solver features tabulated chemistry (Sec. 3.1) with heat losses implementation through EGR dimension (Sec. 3.2), coupled with the ATF approach to model SGS-TCI (Sec. 3.4), and solves an additional transport equation for CO to consider local transport effects (Sec. 3.3). This transported CO quantity is further corrected through an ATF post-processing correction (Sec. 3.5) that considers the impact of flame thickening into the species profiles and flame wrinkling. An offline CHT approach outlined in Sec. 4.2 is utilized to prescribe isothermal conditions to the fluid

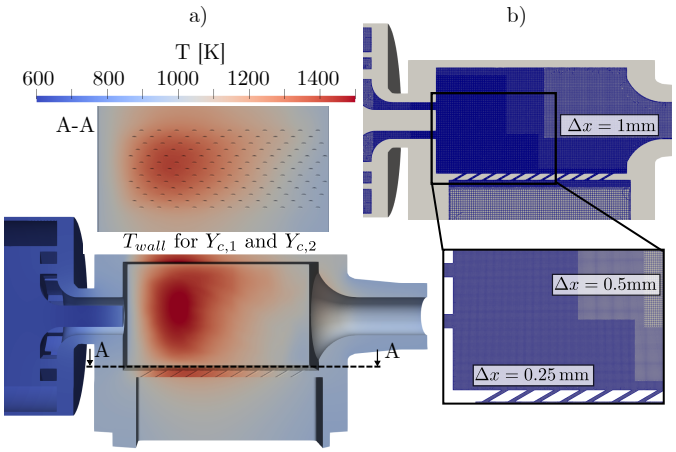

FIGURE 4: *a*) TEMPERATURE DISTRIBUTION IN THE SOLID DOMAIN. *b*) GRID USED IN THE STUDY.

simulation. The isothermal conditions are shown by a cut through the solid domain in Fig.4-a). At the inlets, the mass flows from tab. 1, and a zero gradient condition for pressure are set. The composition of the unburned mixture and pure air are set for the main and cooling flow, respectively. At the outlet, a fixed back pressure (0.25 MPa) and zero gradient for the other quantities are set. The fluid domain is discretized with a hex-dominant grid with 54 M, shown in Fig. 4-b). Local refinements have been introduced to ensure the correct resolution of turbulent structures. In the fluid, the maximum cell size is $\Delta x = 2$ mm in the intake section. In the swirler, it is refined to $\Delta x = 0.5$ mm. The flame zone and effusion cooling plate feature cells with $\Delta x = 0.25$ mm. This value was chosen to give a thickening factor $\mathcal{F} < 10$ with $n = 5$ in the flame front, which leads to values of $\mathcal{F}_{\max} \approx 7$ in the simulation. Downstream, the grid size increases to $\Delta x = 0.5$ mm. It reaches $\Delta x = 1$ mm close to the outlet.

This mesh is the result of a grid convergence study. A coarse mesh with 4 M cells showed flashback and generally a wrong flow field. For an intermediate mesh with $\Delta x = 0.5$ mm (24 M) in the flame area and hence $\mathcal{F}_{\max} \approx 15$, the global flowfield quantities, such as temperature and velocity, were properly captured as they are less sensitive to mesh resolution [50], but predictions on CO emissions were unsatisfactory and needed of further mesh refinements -results not included for the sake of brevity-. All results shown are recorded on the fine grid with 54 M cells.

The timestep is dynamically adapted to limit the CFL number to a maximum value of 0.8, which in the flame zone means $CFL_{\max} = 0.3$ during the simulation, corresponding roughly to a timestep of $\Delta t = 2.5 \cdot 10^{-7}$ s. Each fluid simulation took approximately 0.5 M core hours.

4.2 Conjugate Heat Transfer

The temperature conditions on the walls have a strong influence on flame stabilization, flame dynamics, and also possibly on emissions such as CO due to the strong temperature dependency of the CO source and sink terms [51, 52]. As temperature measurements in optically inaccessible regions are not possible, CHT simulations were performed.

An offline CHT approach is utilized here to give reasonable wall temperature estimations in the entire burner [53].

The solid geometry is a simplification of the experimental setup and is shown in Fig. 4-a), along with the final temperature distribution.

Heat transfer and emissivity coefficients for the outer walls are estimated from [12] and previous work on a gas turbine combustor with optical access [54]. Material properties for the solid [14] are assumed constant for a reference temperature of 1073 K, corresponding to the average temperature in the solid around the chamber (see Fig. 4-a)) . The CHT was performed with $Y_{c,1}$. The simulation with $Y_{c,2}$ utilized the same wall temperatures for comparability , but as seen in Fig. 7 and 8 there is little impact of the Y_c choice on the temperature.

The solid domain was discretized with 11 Mio. cells.

The solid simulations required to reach the steady temperature distribution amount to roughly 2000 core hours combined.

The fluid simulation is initially run with isothermal temperatures, and the heat flux from the walls is averaged for 15 ms. Afterwards, the averaged heat flux is used as a Neumann boundary condition to simulate the solid domain. This simulation is run until a steady state is reached. The resulting temperature is mapped to the fluid domain, which is rerun. After a few iterations, a steady temperature is reached.

5. RESULTS AND DISCUSSION

In this section, the LES results for both progress variable definitions $Y_{c,1} = CO_2$ and $Y_{c,2} = CO_2 + H_2O + CO$ are compared against the experimental data. Before investigating the effect of the different modeling extensions for predicting CO emissions, the global features of the effusion cooling configurations are discussed and validated with the available experimental data.

5.1 Temperature and velocity fields

In Fig.5, the time-averaged velocity and temperature, CO mass-fraction, and normalized mixture fraction fields on the center slice of the lower half of the combustor are shown. The v-shaped flame stabilizes near the swirler exit, and its lower branch interacts with the first holes of the effusion cooling plate. Four distinct zones of interaction can be identified: the inner recirculation zone (IRZ), the inner shear layer (ISL), the outer shear layer (OSL), and the outer recirculation zone (ORZ).

Regarding the OSL and ORZ and as noted from the Z contour, there is an increased penetration depth, leading to an enhanced chemical interaction between the cooling air and the recirculated hot products[13]. Downstream, the process is dominated by dilution with increased cooling flow through the additional effusion cooling holes. This results in a decrease in temperature in the axial direction close to the wall. The 50 % dilution isoline illustrates that a full cooling film is only developed after the fourth effusion cooling hole. The hot combustion products

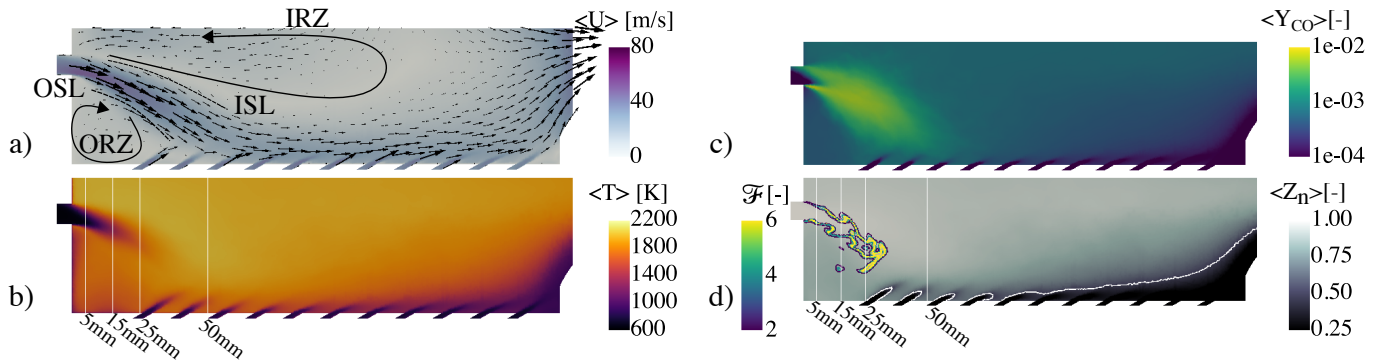

FIGURE 5: TIME AVERAGED VELOCITY, TEMPERATURE, TRANSPORTED CO MASS FRACTION AND NORMALIZED MIXTURE FRACTION FIELDS. FLOW STRUCTURES MARKED IN BLACK OVER THE VELOCITY FIELD. WHITE LINES MARK THE POSITION OF VERTICAL LINE COMPARISONS. 50 % DILUTION ISOLINE SHOWN OVER Z_n IN WHITE. INSTANTANEOUS $\mathcal{F}$ ISOLINES PLOTTED OVER Z_n.

interact with the incoming cooling flow between the second and fourth effusion cooling holes.

The IRZ features higher temperatures than the ORZ due to the heat-loss effects on the wall through chemical quenching and effusion cooling flow recirculation for the ORZ. The OSL shows a strong mixing with the cooling flow and the possible influence of the boundary condition at the cooling plate, which explains its lower temperatures compared to the ISL.

In the following, the simulation results are compared against the available experimental data at vertical lines indicated in Fig. 5-b . Both $Y_{c,1}$ and $Y_{c,2}$ show nearly identical mean profiles for the average velocity and temperature field. Thus, only results for $Y_{c,1}$ are discussed for brevity.

For a qualitative comparison of the flow field, the mean and Root-Mean-Square (RMS), of axial and radial velocity are compared in Fig. 6 at different axial distances from the swirler exit ($x \in [5, 15, 15]$ mm) to the PIV data [25]. The PIV data was recorded for a lower equivalence ratio ($\varphi = 0.65$ [25]), which was accounted for by the simulations used for this comparison. The simulation features a higher peak at $x = 15$ mm. The peak in axial and radial velocities is slightly shifted inwards. RMS profiles match well for both axial and radial velocities, indicating that turbulent fluctuations are accurately captured by the LES.

In Fig.7, the time-averaged temperature profiles are compared along the axial direction of the combustion chamber. The experimental data was recorded for the same operating point [13], so they are directly comparable.

At $x = 5$ mm, simulation and measurement are in good agreement. The low-temperature peak at $z = -20$ mm, coincident with the fresh gases injection, as well as the rise in temperature in the ISL and OSL, are well predicted. At the following profiles at $x = 15$ mm and $x = 25$ mm, the simulations show higher temperatures in the main flow jet region, indicating faster fuel consumption in the simulation compared to the experiment. At $x = 50$ mm, the profiles are again in good agreement. This is the axial position at which the main flow starts to impinge on the cooling jets.

In Fig.8, the time-averaged horizontal temperature profiles at different heights over the effusion cooling plate z_w are compared against the experimental data.

The general shape of the temperature profile and level of the experimental measurement are reproduced by the simulations. However, especially at $z_w = 1.5$ mm, the individual effusion cooling jets are visible as regions of lower temperature. This suggests that the jet penetration lengths around the effusion cooling area are slightly overestimated by the simulation. This might be caused by different factors: uncertainties in the experimentally estimated cooling flow temperature or mass flows, overestimation of the numerical wall temperatures in the effusion holes, or overestimated boundary layer sizes in the holes leading to higher velocity peaks. At $z_w = 3$ mm, the jets coming from the second and third effusion cooling hole are also apparent.

From the previous comparisons, it can be noted that the choice of Y_c definition has little impact on the general flow field. Both simulations give identical predictions for both flow-field and temperature distributions in the primary zone and the FCAI area.

5.2 CO formation during FCAI

While the global flow field is well predicted regardless of Y_c choice, it is unclear if the same holds for CO predictions. Furthermore, the effect of the split formulation in $\dot{\omega}_{\mathrm{CO}}$ (Sec. 3.3) is analyzed for $Y_{c,1}$ and $Y_{c,2}$. Lastly, the ATF correction (Sec. 3.5) is evaluated in a close-to-reality effusion cooling chamber.

In Fig. 9, the CO profiles on the vertical lines marked in Fig. 5-d are presented. Both the direct table lookup of $\dot{\omega}_{CO}^{table}$ and the split into production and destruction terms from Eq. (2) is shown. At first, the effect of the ATF correction is discussed for the split-based formulation (right column). As the investigated vertical lines ($x \in [5, 15, 25]$ mm) intersect with the flame and thus thickened regions (see Fig. 5-d, instantaneous isolines of $\mathcal{F}$), average transported CO profiles are overpredicted for both Y_c definitions (black and grey) at all positions. Applying the ATF-post-correction for transported CO from (5) results in near identical profiles for both simulations at all positions. Sim-

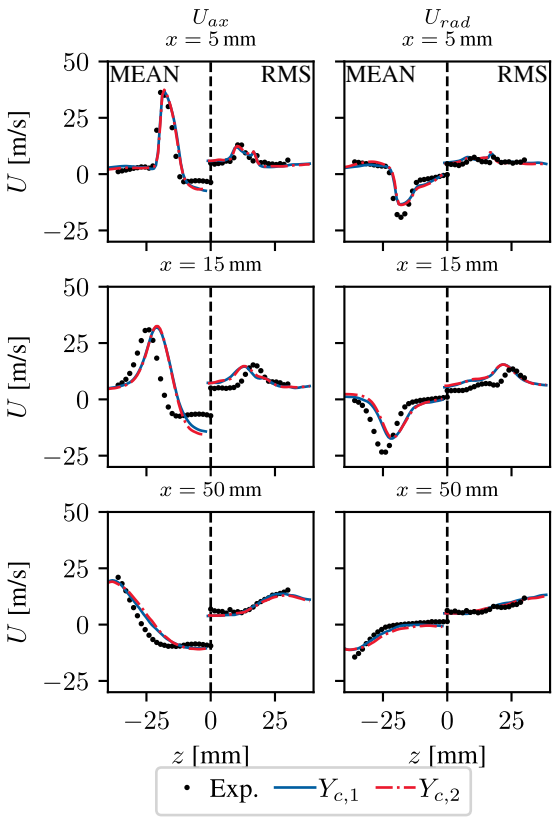

FIGURE 6: MEAN AND RMS AXIAL (LEFT) AND RADIAL (RIGHT) VELOCITY PROFILES.

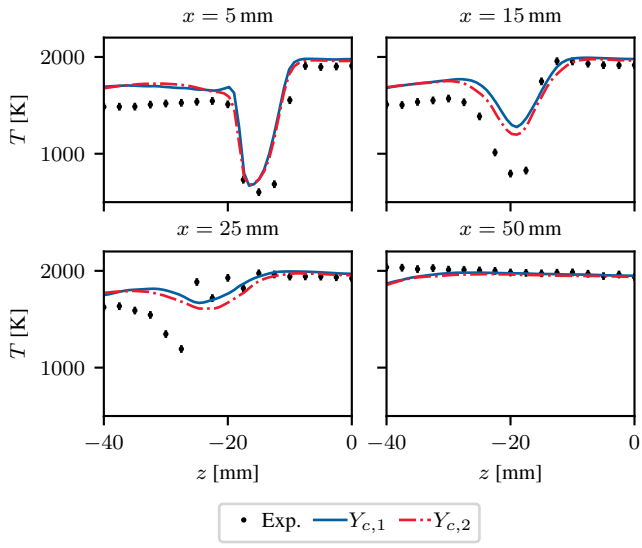

FIGURE 7: MEAN TEMPERATURE PROFILES ALONG THE AXIAL DIRECTION.

ulations and experimental data agree well for $x = 25$ mm. At $x = 15$ mm, the simulations result in too low CO values. The peak in CO is also shifted towards the lower wall due to the over-estimation of ORZ temperature. At $x = 5$ mm, the peaks are over-predicting CO, which might be caused by an altered flame anchoring behavior. Regardless of the chosen progress variable and correction, the CO values in the IRZ are underpredicted, due to long residence times and the recirculation from the top wall, where thermal quenching is dominant. To summarize, the ATF correction works well if applied to transported CO values at elevated pressures, which holds not just for $Y_{c,2}$ for which it was originally developed at atmospheric conditions [45], but also for $Y_{c,1}$.

Now the effects of the $\dot{\omega}_{CO}$ treatment are discussed for both Y_c definitions. Only the turbulent corrected profiles are discussed for brevity. As mentioned before, the split-based formulation (right column) results in good agreement between $Y_{c,1}$ and $Y_{c,2}$. Without the split formulation $Y_{c,1}$ gives similar results as with the split formulation. For $Y_{c,2}$ using $\dot{\omega}_{CO}^{table}$ directly results in severe underpredictions at both $x = 15$ mm ,and $x = 25$ mm, although the general shape is roughly captured. The drastic improvement of $Y_{c,2}$ and the minor differences for $Y_{c,1}$ with the split formulation can be explained by the CO-source terms in Fig. 3. For $Y_{c,2}$, the negative peak in $\dot{\omega}_{\mathrm{CO}}$ is in a very narrow region of $Y_c \in [0.9, 1]$, which is not well resolved by the table. Splitting this term into production $\dot{\omega}_{\mathrm{CO}}^{+}$ and destruction $\dot{\omega}_{\mathrm{CO}}^{-}$ terms widens these profiles and removes the zero crossing making the profiles better resolved by the table. For $Y_{c,1}$, all three CO source terms are smooth and span a much wider Y_c range. Furthermore, they are better aligned with $\dot{\omega}_{Y_c}$. Thus $Y_{c,1}$ results in better performance without the split-based formulation. Similar results might be obtainable with a refined table for $Y_{c,2}$, but these are more costly and harder to construct for a wide enthalpy and mixture fraction range.

In Fig. 10, the time-averaged CO mole fraction profiles are plotted for different wall distances z_w over the cooling plate and compared with the experimental data for both progress variables and with and without the split formulation of $\dot{\omega}_{CO}$. As the flame and thus thickening effects do not appear close to the wall (Fig.5-d)), there is no need for the CO-ATF post-processing correction. Especially at $z_w = 1.5$ mm, the influence of the ISL, OSL, and ORZ on CO emissions can be observed in the experimental profiles. At $x = 30$ mm, the first cooling jet flow penetrates and interacts with the ORZ and OSL, leading to an increased chemical quenching of the late CO oxidation branch and to the first maximum of X_{CO} in the measured profile. Further downstream, there is a minimum of X_{CO} next to the second cooling hole position, with the influence of more diluted ISL and OSL with an increase in cooling rate flow. From this point, X_{CO} increases linearly, which is caused by the convective transport of exhaust products from the ISL towards the cooling liner. A maximum is reached at $x \approx 65$ mm, coinciding with the fourth cooling hole location. Subsequently, X_{CO} continually decreases monotonically due to the development of a continuous cooling film and enhanced dilution from this axial position (see 50 % dilution line in Fig. 5).

When analyzing the differences between both Y_c definitions

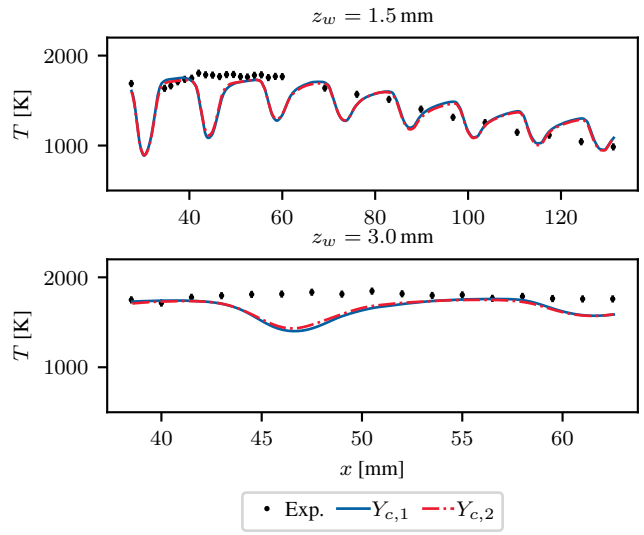

FIGURE 8: HORIZONTAL TEMPERATURE PROFILES AT DIFFERENT HEIGHTS z_w OVER THE EFFUSION COOLING PLATE.

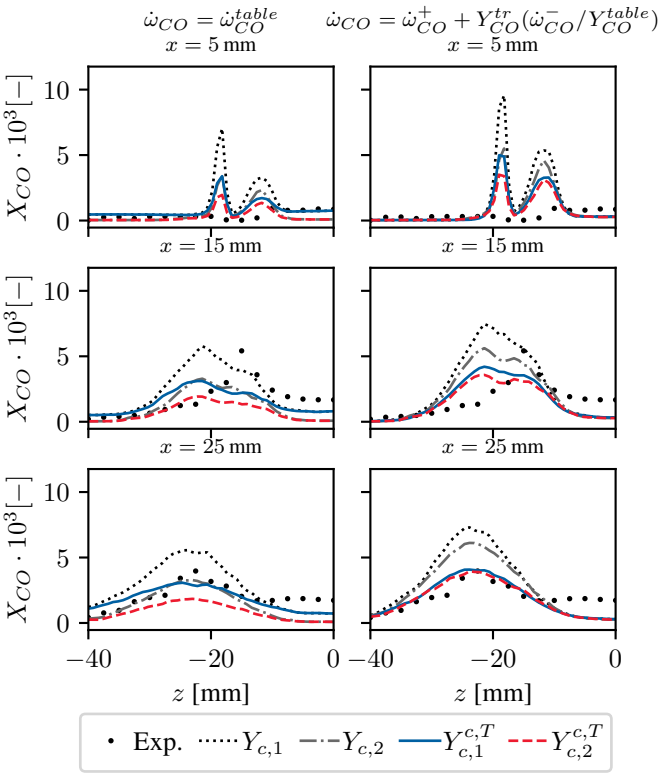

FIGURE 9: MEAN CO PROFILES IN AXIAL DIRECTION WITH (RIGHT) AND WITHOUT (LEFT) SOURCE TERM SPLITTING FOR $\dot{\omega}_{CO}$, EQ. (2).

without the split of $\dot{\omega}_{CO}$, similar results are observed as in the vertical lines. Due to the bad resolution of the source term for

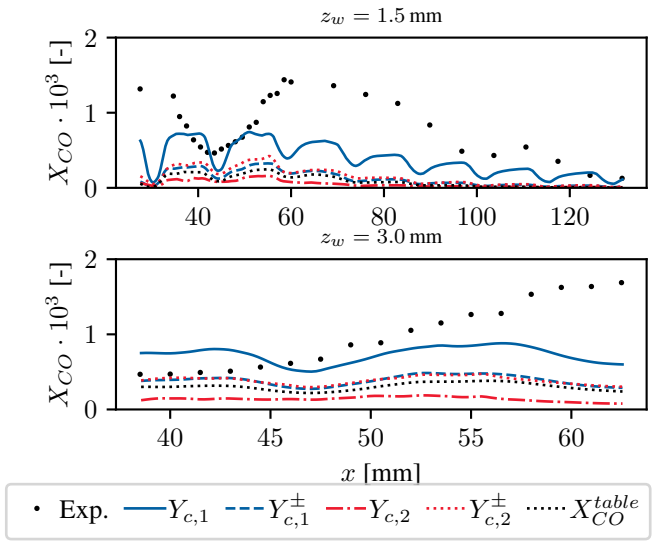

FIGURE 10: HORIZONTAL CO PROFILES AT DIFFERENT HEIGHTS z_w OVER THE EFFUSION COOLING PLATE.

$Y_{c,2}$ CO is severely underpredicted. For $Y_{c,1}$, a better agreement is observed, but the profiles are not captured. Furthermore, at z_w = 1.5 mm, the individual cooling jets are visible as minima in X_{CO} concentration. When analyzing the split formulation $\dot{\omega}_{CO}^{\pm}$, both Y_c simulations result in very low CO predictions. This is due to the linear scaling of the destruction term in (2). Close to the wall, the transported CO is one to two orders of magnitudes larger than the tabulated value. Thus, the destruction term is overestimated, resulting in the CO_{trans} to be very close to the tabulated CO_{table} values, which are indicated as the black dotted line in the plots. Thus close to the wall, the split formulation no longer works as transported and tabulated CO values diverge radically in these regions.

In general, the CO modeling becomes more challenging closer to the effusion plate than in less dilution-affected areas. The reasons are the stronger interactions of mixing, heat losses, and chemical reactions. Besides, there may be an overlap with heat loss-induced flame quenching with the wall, especially before the fourth hole and cooling film formation, which might require more advanced chemistry tabulation techniques [21]. Additionally, the high temperatures in some parts of the cooling plate ($\approx$ 1300 K) are above the auto-ignition temperature, which could affect the CO predictions from flamelet-manifold models in general and would equally require more advanced models. The strong transport effects furthermore limit the applicability of previous corrections, such as the linear scaled destruction term, due to the large discrepancy between the tabulated and transported states.

6. CONCLUSIONS

In the present study, a practically relevant effusion-cooled single-sector model gas turbine combustor was investigated by using a LES-ATF approach coupled with tabulated chemistry based on premixed flamelets. Temperature boundary conditions

were computed via CHT. Model sensitivities to the progress variable definition, the split and linear correction of the CO source term in an additional transport equation for CO, and a CO post-processing correction for ATF were thoroughly assessed.

This work demonstrates the capabilities of LES coupled with premixed tabulated chemistry to accurately model global effects in a laboratory-scale configuration. Temperature and velocity profiles were well captured.

Regarding the CO modeling sensitivities following conclusions are drawn:

- Two different progress variable definitions were considered, $Y_{c,1} = CO_2$ and $Y_{c,2} = CO_2 + H_2O + CO$. In the primary zone, $Y_{c,1}$ showed a better performance than $Y_{c,2}$ when $\dot{\omega}_{\mathrm{CO}}$ is read from the table.
- The split and linear correction in $\dot{\omega}_{CO}$ effectively reconciled the difference between $Y_{c,1}$ and $Y_{c,2}$, notably improving $Y_{c,2}$ predictions. The split's benefits are linked to enhanced resolution of production and destruction terms in the $Y_{c,2}$ table, whereas $Y_{c,1}$ displays broader source term profiles regardless of the splitting method. In the FCAI region, the linear scaling of the destruction term results in profiles closer to tabulated values for both Y_c definitions. Thus, the tested split shows minor influence compared to tabulated values near walls when combined with EGR tables, as transported CO deviates significantly from tabulated values.
- The CO-ATF post-processing correction successfully reduced the overestimation in numerical predictions and aligned further the simulation and experimental data.
- Integrating EGR effects into the flamelet tables holds the potential to enhance accuracy in the FCAI region. Despite a reasonable agreement between experimental and numerical thermo-chemical states (CO-T), addressing near-wall issues could benefit from recently advanced manifolds with flame-quenching effects and considerations of mixing, dilution phenomena [32, 33], along with extensions to high wall temperatures encountered in gas turbine combustors.

This thorough evaluation of submodels underscores the significance of meticulous model selection, as the overall modeling error is influenced by the weakest link. These insights can guide future studies on modeling CO emissions in aero-engines and stationary gas turbines.

ACKNOWLEDGMENT

The authors kindly acknowledge financial support through the Federal Ministry of Education and Research under the Federal Aeronautical Research Program (LuFo VI, Call 1). The authors gratefully acknowledge the funding by the aforementioned institution, the ongoing support of Ruud Eggels and Max Staufer from Rolls-Royce Deutschland, and the computing time provided to them on the high-performance computer Lichtenberg at the NHR Centers NHR4CES at TU Darmstadt. This is funded by the Federal Ministry of Education and Research, and the state governments participating on the basis of the resolutions of the GWK for national high-performance computing at universities.

REFERENCES

[1] Boeing. "Current Market Outlook 2016-2035." (2016).

[2] Directorate-General for Mobility and Transport (European Commision) and Directorate-General for Research and Innovation (European Commision). *Flightpath 2050 Europe's vision for aviation* (2011). DOI 10.2777/50266.

[3] Angersbach, A., Bestie, D. and Eggels, R. "Automated combustor preliminary design using tools of different fidelity." *Proceedings of the ASME Turbo Expo* Vol. 1 A (2013): pp. 1–8. DOI 10.1115/GT2013-94411.

[4] Eggels, R. L. G. M. "The Application of Combustion LES Within Industry." Grigoriadis, D. G.E., Geurts, B. J., Kuerten, H., Froehlich, J. and Armenio, V. (eds.). *Direct and Large-Eddy Simulation X*: pp. 3–13. 2018. Springer International Publishing.

[5] Popp, S. *Large Eddy Simulation of Turbulent Multi-regime Combustion: Potentials and Limitations of Flamelet-based Chemistry Modeling*. Verlag Dr. Hut (2020).

[6] Popp, S., Hartl, S., Butz, D., Geyer, D., Dreizler, A., Vervisch, L. and Hasse, C. "Assessing multi-regime combustion in a novel burner configuration with large eddy simulations using tabulated chemistry." *Proc. Combust. Inst.* Vol. 38 No. 2 (2021): pp. 2551–2558. DOI 10.1016/j.proci.2020.06.098.

[7] Koob, P., Ferraro, F., Nicolai, H., Eggels, R., Staufer, M. and Hasse, C. "Large Eddy Simulation of Soot Formation in a Real Aero-Engine Combustor Using Tabulated Chemistry and a Quadrature-Based Method of Moments." *J. Eng. Gas Turbine. Power* Vol. 146 No. 1 (2024): p. 011015. DOI 10.1115/1.4063376.

[8] Haselbach, F., Newby, A. and Parker, R. "Concepts and technologies for the next generation of large civil aircraft engines." *Proceedings of the ICAS Gas Turbine India Conference - 2013*: pp. –. St. Petersburg, Russia, 2014-09-07/2014-09-12, 2014.

[9] Behrendt, T. and Hassa, C. "A test rig for investigations of gas turbine combustor cooling concepts under realistic operating conditions." *Proceedings of the Institution of Mechanical Engineers, Part G: Journal of Aerospace Engineering* Vol. 222 No. 2 (2008): pp. 169–177. DOI 10.1243/09544100JAERO288.

[10] Schulz, A. "Combustor Liner Cooling Technology in Scope of Reduced Pollutant Formation and Rising Thermal Efficiencies." *Ann. N.Y. Acad. Sci.* Vol. 934 No. 1 (2001): pp. 135–146. DOI 10.1111/j.1749-6632.2001.tb05848.x.

[11] Klarmann, N., Zoller, B. T. and Sattelmayer, T. "Modeling of CO Emissions in Multi-Burner Systems With Fuel Staging." *Volume 4A: Combustion, Fuels, and Emissions*: p. V04AT04A049. 2019. American Society of Mechanical Engineers, Phoenix, Arizona, USA. DOI 10.1115/GT2019-90821.

[12] Greifenstein, M., Hermann, J., Boehm, B. and Dreizler, A. "Flame–cooling air interaction in an effusion-cooled model gas turbine combustor at elevated pressure." *Exp. Fluids* Vol. 60 No. 1 (2019): p. 10. DOI 10.1007/s00348-018-2656-3.

[13] Greifenstein, M. and Dreizler, A. "Influence of effusion cooling air on the thermochemical state of combustion in a pressurized model single sector gas turbine combustor." *Combust. Flame* Vol. 226 (2021): pp. 455–466. DOI 10.1016/j.combustflame.2020.12.031.

[14] Greifenstein, M. "Experimental investigations of flame-cooling air interaction in an effusion cooled pressurized single sector model gas turbine combustor." Ph.D. Thesis, TU Darmstadt. 2021. DOI 10.26083/TUPRINTS-00019205.

[15] Greifenstein, M. and Dreizler, A. "Influence of effusion cooling air on the CO production in the primary zone of a pressurized single sector model gas turbine combustor." *Combust. Flame* Vol. 248 (2023): p. 112511. DOI 10.1016/j.combustflame.2022.112511.

[16] Efimov, D. V., De Goey, P. and Van Oijen, J. A. "QFM: quenching flamelet-generated manifold for modelling of flame–wall interactions." *Combust. Theory Model.* Vol. 24 No. 1 (2020): pp. 72–104. DOI 10.1080/13647830.2019.1658901.

[17] Steinhausen, M., Luo, Y., Popp, S., Strassacker, C., Zirwes, T., Kosaka, H., Zentgraf, F., Maas, U., Sadiki, A., Dreizler, A. and Hasse, C. "Numerical Investigation of Local Heat-Release Rates and Thermo-Chemical

States in Side-Wall Quenching of Laminar Methane and Dimethyl Ether Flames." *Flow Turbul. Combust.* Vol. 106 No. 2 (2021): pp. 681–700. DOI 10.1007/s10494-020-00146-w.

[18] Oijen, J.A. Van and Goey, L.P.H. De. "Modelling of Premixed Laminar Flames using Flamelet-Generated Manifolds." *Combust. Sci. Technol.* Vol. 161 No. 1 (2000): pp. 113–137. DOI 10.1080/00102200008935814.

[19] Ketelheun, A., Olbricht, C., Hahn, F. and Janicka, J. "Premixed Generated Manifolds for the Computation of Technical Combustion Systems." *Volume 2: Combustion, Fuels and Emissions*: pp. 695–705. 2009. ASMEDC, Orlando, Florida, USA. DOI 10.1115/GT2009-59940.

[20] Han, W., Wang, H., Kuenne, G., Hawkes, E. R., Chen, J. H., Janicka, J. and Hasse, C. "Large eddy simulation/dynamic thickened flame modeling of a high Karlovitz number turbulent premixed jet flame." *Proc. Combust. Inst.* Vol. 37 No. 2 (2019): pp. 2555–2563. DOI 10.1016/j.proci.2018.06.228.

[21] Ganter, S., Heinrich, A., Meier, T., Kuenne, G., Jainski, C., Rißmann, M. C., Dreizler, A. and Janicka, J. "Numerical analysis of laminar methane–air side-wall-quenching." *Combust. Flame* Vol. 186 (2017): pp. 299–310. DOI 10.1016/j.combustflame.2017.08.017.

[22] Ketelheun, A., Kuenne, G. and Janicka, J. "Heat Transfer Modeling in the Context of Large Eddy Simulation of Premixed Combustion with Tabulated Chemistry." *Flow Turbul. Combust.* Vol. 91 No. 4 (2013): pp. 867–893. DOI 10.1007/s10494-013-9492-6.

[23] Palulli, R., Brouzet, D., Talei, M. and Gordon, R. L. "A comparative study of flame-wall interaction and flame-cooling air interaction." *Int J Heat Fluid Flow* Vol. 92 (2021): p. 108888. DOI 10.1016/j.ijheatfluidflow.2021.108888.

[24] Palulli, R., Talei, M. and Gordon, R. L. "Analysis of Near-Wall CO due to Unsteady Flame-Cooling Air Interaction." *Flow Turbul. Combust.* Vol. 107 No. 2 (2021): pp. 343–365. DOI 10.1007/s10494-020-00233-y.

[25] Hermann, J. "Laseroptische Untersuchung der Flamme-Kühlluft-Interaktion in einer effusionsgekühlten Brennkammer." Ph.D. Thesis, TU Darmstadt. 2017.

[26] Amerini, A., Paccati, S., Mazzei, L. and Andreini, A. "Assessment of a Conjugate Heat Transfer Method on an Effusion Cooled Combustor Operated With a Swirl Stabilized Partially Premixed Flame." *J. Turbomach. Trans. ASME* Vol. 145 No. 8 (2023): p. 081007. DOI 10.1115/1.4056983.

[27] Heeger, C. *Flashback investigations in a premixed swirl burner by high-speed laser imaging*. No. 601 in *Fortschritt-Berichte VDI, Reihe 6, Energietechnik*, VDI Verlag GmbH, Düsseldorf, Deutschland (2012). Darmstadt, TU, Diss., 2011.

[28] Goodwin, D. G., Moffat, H. K., Schoegl, I., Speth, R. L. and Weber, B. W. "Cantera: An Object-oriented Software Toolkit for Chemical Kinetics, Thermodynamics, and Transport Processes." https://www.cantera.org (2023). DOI 10.5281/zenodo.8137090. Version 3.0.0.

[29] Fiorina, B., Mercier, R., Kuenne, G., Ketelheun, A., Avdić, A., Janicka, J., Geyer, D., Dreizler, A., Alenius, E., Duwig, C., Trisjono, P., Kleinheinz, K., Kang, S., Pitsch, H., Proch, F., Cavallo Marincola, F. and Kempf, A. "Challenging modeling strategies for LES of non-adiabatic turbulent stratified combustion." *Combust. Flame* Vol. 162 No. 11 (2015): pp. 4264–4282. DOI 10.1016/j.combustflame.2015.07.036.

[30] Fiorina, B., Luu, T. P., Dillon, S., Mercier, R., Wang, P., Angelilli, L., Ciottoli, P. P., Hernández–Pérez, F. E., Valorani, M., Im, H. G., Massey, J. C., Li, Z., Chen, Z. X., Swaminathan, N., Popp, S., Hartl, S., Nicolai, H., Hasse, C., Dreizler, A., Butz, D., Geyer, D., Breicher, A., Zhang, K., Duwig, C., Zhang, W., Han, W., Van Oijen, J., Péquin, A., Parente, A., Engelmann, L., Kempf, A., Hansinger, M., Pfitzner, M. and Barlow, R. S. "A joint numerical study of multi-regime turbulent combustion." *Appl. Energy Combust. Sci.* Vol. 16 (2023): p. 100221. DOI 10.1016/j.jaecs.2023.100221.

[31] Smith, G. P., Golden, D. M., Frenklach, M., Moriarty, N. W., Eiteneer, B., Goldenberg, M., Bowman, C. T., Hanson, R. K., Song, S., Jr., W. C. Gardiner, Lissianski, V. V. and Qin, Z. "GRI 3.0 reaction mechanism." URL http://www.me.berkeley.edu/gri_mech/.

[32] Steinhausen, M., Zirwes, T., Ferraro, F., Scholtissek, A., Bockhorn, H. and Hasse, C. "Flame-vortex interaction during turbulent side-wall quenching and its implications for flamelet manifolds." *Proc. Combust. Inst.* Vol. 39 No. 2 (2023): pp. 2149–2158. DOI 10.1016/j.proci.2022.09.026.

[33] Luo, Y., Steinhausen, M., Kaddar, D., Hasse, C. and Ferraro, F. "Assessment of flamelet manifolds for turbulent flame-wall interactions in large-eddy simulations." *Combust. Flame* Vol. 255 (2023): p. 112923. DOI 10.1016/j.combustflame.2023.112923.

[34] Fiorina, B., Baron, R., Gicquel, O., Thevenin, D., Carpentier, S. and Darabiha, N. "Modelling non-adiabatic partially premixed flames using flame-prolongation of ILDM." *Combust. Theory Model.* Vol. 7 No. 3 (2003): pp. 449–470. DOI 10.1088/1364-7830/7/3/301.

[35] Van Oijen, J.A., Donini, A., Bastiaans, R.J.M., Ten Thije Boonkkamp, J.H.M. and De Goey, L.P.H. "State-of-the-art in premixed combustion modeling using flamelet generated manifolds." *Prog. Energy Combust. Sci.* Vol. 57 (2016): pp. 30–74. DOI 10.1016/j.pecs.2016.07.001.

[36] Nicolai, H., Kuenne, G., Knappstein, R., Schneider, H., Becker, L.G., Hasse, C., Mare, F. Di, Dreizler, A. and Janicka, J. "Large Eddy Simulation of a laboratory-scale gas-assisted pulverized coal combustion chamber under oxy-fuel atmospheres using tabulated chemistry." *Fuel* Vol. 272 (2020): p. 117683. DOI 10.1016/j.fuel.2020.117683.

[37] Ihme, M. and Pitsch, H. "Modeling of radiation and nitric oxide formation in turbulent nonpremixed flames using a flamelet/progress variable formulation." *Physics of Fluids* Vol. 20 No. 5 (2008): p. 055110. DOI 10.1063/1.2911047.

[38] Ketelheun, A., Olbricht, C., Hahn, F. and Janicka, J. "NO prediction in turbulent flames using LES/FGM with additional transport equations." *Proceedings of the Combustion Institute* Vol. 33 No. 2 (2011): pp. 2975–2982. DOI 10.1016/j.proci.2010.07.021.

[39] Mueller, M. E. and Pitsch, H. "LES model for sooting turbulent nonpremixed flames." *Combust. Flame* Vol. 159 No. 6 (2012): pp. 2166–2180. DOI 10.1016/j.combustflame.2012.02.001.

[40] Kuenne, G., Ketelheun, A. and Janicka, J. "LES modeling of premixed combustion using a thickened flame approach coupled with FGM tabulated chemistry." *Combust. Flame* Vol. 158 No. 9 (2011): pp. 1750–1767. DOI 10.1016/j.combustflame.2011.01.005.

[41] Charlette, F., Meneveau, C. and Veynante, D. "A power-law flame wrinkling model for LES of premixed turbulent combustion Part I: non-dynamic formulation and initial tests." *Combust. Flame* Vol. 131 No. 1-2 (2002): pp. 159–180. DOI 10.1016/S0010-2180(02)00400-5.

[42] Kuenne, G., Seffrin, F., Fuest, F., Stahler, T., Ketelheun, A., Geyer, D., Janicka, J. and Dreizler, A. "Experimental and numerical analysis of a lean premixed stratified burner using 1D Raman/Rayleigh scattering and large eddy simulation." *Combust. Flame* Vol. 159 No. 8 (2012): pp. 2669–2689. DOI 10.1016/j.combustflame.2012.02.010.

[43] Durand, L. and Polifke, W. "Implementation of the Thickened Flame Model for Large Eddy Simulation of Turbulent Premixed Combustion in a Commercial Solver." *Volume 2: Turbo Expo 2007*: pp. 869–878. 2007. ASMEDC, Montreal, Canada. DOI 10.1115/GT2007-28188.

[44] Vervisch, L., Domingo, P., Lodato, G. and Veynante, D. "Scalar energy fluctuations in Large-Eddy Simulation of turbulent flames: Statistical budgets and mesh quality criterion." *Combust. Flame* Vol. 157 No. 4 (2010): pp. 778–789. DOI 10.1016/j.combustflame.2009.12.017.

[45] Gruhlke, P., Inanc, E., Mercier, R., Fiorina, B. and Kempf, A. M. "A simple post-processing method to correct species predictions in artificially thickened turbulent flames." *Proc. Combust. Inst.* Vol. 38 No. 2 (2021): pp. 2977–2984. DOI 10.1016/j.proci.2020.06.215.

[46] Moureau, V., Domingo, P. and Vervisch, L. "From Large-Eddy Simulation to Direct Numerical Simulation of a lean premixed swirl flame: Filtered laminar flame-PDF modeling." *Combust. Flame* Vol. 158 No. 7 (2011): pp. 1340–1357. DOI 10.1016/j.combustflame.2010.12.004.

[47] Mercier, R., Mehl, C., Fiorina, B. and Moureau, V. "Filtered Wrinkled Flamelets model for Large-Eddy Simulation of turbulent premixed combustion." *Combust. Flame* Vol. 205 (2019): pp. 93–108. DOI 10.1016/j.combustflame.2019.03.025.

[48] Weller, H. G., Tabor, G., Jasak, H. and Fureby, C. "A tensorial approach to computational continuum mechanics using object-oriented techniques." *Computers in Physics* Vol. 12 No. 6 (1998): pp. 620–631. DOI 10.1063/1.168744.

[49] Nicoud, F., Toda, H. B., Cabrit, O., Bose, S. and Lee, J. "Using singular values to build a subgrid-scale model for large eddy simulations." *Phys. Fluids* Vol. 23 No. 8 (2011): p. 085106. DOI 10.1063/1.3623274.

,
[50] Boudier, G., Gicquel, L.Y.M. and Poinsot, T.J. "Effects of mesh resolution on large eddy simulation of reacting flows in complex geometry combustors." *Combust. Flame* Vol. 155 No. 1-2 (2008): pp. 196–214. DOI 10.1016/j.combustflame.2008.04.013.

[51] Shahi, M., Kok, J. B.W., Roman Casado, J.C. and Pozarlik, A. K. "Transient heat transfer between a turbulent lean partially premixed flame in limit cycle oscillation and the walls of a can type combustor." *Appl. Therm. Eng.* Vol. 81 (2015): pp. 128–139. DOI 10.1016/j.applthermaleng.2015.01.060.

[52] Agostinelli, P.W., Laera, D., Boxx, I., Gicquel, L. and Poinsot, T. "Impact of wall heat transfer in Large Eddy Simulation of flame dynamics in a swirled combustion chamber." *Combust. Flame* Vol. 234 (2021): p. 111728. DOI 10.1016/j.combustflame.2021.111728.

[53] Karpowski, T. J. P., Ferraro, F., Steinhausen, M., Popp, S., Arndt, C. M., Kraus, C., Bockhorn, H., Meier, W. and Hasse, C. "Numerical Investigation of the Local Thermo-Chemical State in a Thermo-Acoustically Unstable Dual Swirl Gas Turbine Model Combustor." *Proceedings of the ASME Turbo Expo* Vol. 3 B (2022): pp. 1–10. DOI 10.1115/GT2022-83810.

[54] Arndt, C. M., Nau, P. and Meier, W. "Characterization of wall temperature distributions in a gas turbine model combustor measured by 2D phosphor thermometry." *Proc. Combust. Inst.* (2020): pp. 1867–1875DOI 10.1016/j.proci.2020.06.088.

LIST OF TABLES

LIST OF FIGURES